Parametric study of the physical properties of hydrate-bearing sand, silt, and clay sediments: 2. Small-strain mechanical properties

J. Y. Lee,[1] F. M. Francisca,[2] J. C. Santamarina,[3] and C. Ruppel[4]

Received 5 June 2009; revised 31 May 2010; accepted 8 July 2010; published 9 November 2010.

[1] The small-strain mechanical properties (e.g., seismic velocities) of hydrate-bearing sediments measured under laboratory conditions provide reference values for calibration of logging and seismic exploration results acquired in hydrate-bearing formations. Instrumented cells were designed for measuring the compressional (P) and shear (S) velocities of sand, silts, and clay with and without hydrate and subject to vertical effective stresses of 0.01 to 2 MPa. Tetrahydrofuran (THF), which is fully miscible in water, was used as the hydrate former to permit close control over the hydrate saturation S_{hyd} and to produce hydrate from dissolved phase, as methane hydrate forms in most natural marine settings. The results demonstrate that laboratory hydrate formation technique controls the pattern of P and S velocity changes with increasing S_{hyd} and that the small-strain properties of hydrate-bearing sediments are governed by effective stress, σ'_v and sediment specific surface. The S velocity increases with hydrate saturation owing to an increase in skeletal shear stiffness, particularly when hydrate saturation exceeds $S_{hyd} \approx 0.4$. At very high hydrate saturations, the small strain shear stiffness is determined by the presence of hydrates and becomes insensitive to changes in effective stress. The P velocity increases with hydrate saturation due to the increases in both the shear modulus of the skeleton and the bulk modulus of pore-filling phases during fluid-to-hydrate conversion. Small-strain Poisson's ratio varies from 0.5 in soft sediments lacking hydrates to 0.25 in stiff sediments (i.e., subject to high vertical effective stress or having high S_{hyd}). At $S_{hyd} \geq 0.5$, hydrate hinders expansion and the loss of sediment stiffness during reduction of vertical effective stress, meaning that hydrate-rich natural sediments obtained through pressure coring should retain their in situ fabric for some time after core retrieval if the cores are maintained within the hydrate stability field.

Citation: Lee, J. Y., F. M. Francisca, J. C. Santamarina, and C. Ruppel (2010), Parametric study of the physical properties of hydrate-bearing sand, silt, and clay sediments: 2. Small-strain mechanical properties, *J. Geophys. Res.*, *115*, B11105, doi:10.1029/2009JB006670.

1. Introduction

[2] Both compressional velocity (V_P) and shear velocity (V_S) increase when gas hydrate forms in sediments, as demonstrated by numerous studies conducted with different hydrate formation methods, hydrate forming substances, soils, laboratory cells, and effective stress conditions [*Bathe et al.*, 1984; *Berge et al.*, 1999; *Kiefte et al.*, 1985; *Lee et al.*, 2008; *Pandit and King*, 1982; *Pearson et al.*, 1986; *Priest et al.*, 2005; *Spangenberg and Kulenkampff*, 2005; *Stoll*, 1974; *Stoll and Bryan*, 1979; *Stoll et al.*, 1971; *Winters et al.*, 2005; *Wittebolle and Sego*, 1985]. While the details of these experiments differ, the finding of increasing velocity with increasing hydrate saturation is a consistent result and reflects the impact of hydrate on both the small-strain shear stiffness and the bulk modulus of sediments.

[3] In field settings, seismic velocity data have gained wide applicability in characterizing hydrate-bearing sediments at borehole to regional scales. Borehole sonic logs have often been used to estimate hydrate saturation [e.g., *Tinivella and Carcione*, 2001; *Guerin and Goldberg*, 2002]. Vertical seismic profiling [e.g., *Holbrook et al.*, 1996], ocean bottom cable data [*Hardage et al.*, 2006], and analysis of exploration seismic data using seismic attributes, full waveform inversion, and other approaches [e.g., *Bangs et al.*, 1993; *Bauer et al.*, 2008; *Dai et al.*, 2008; *Korenaga et al.*, 1997; *Kumar et al.*, 2007; *Westbrook et al.*, 2008; *Zillmer*,

[1]Petroleum and Marine Resources Division, Korea Institute of Geoscience and Mineral Resources, Deajeon, South Korea.
[2]Ingenieria Civil, Universidad Nacional de Cordoba, Cordoba, Argentina.
[3]School of Civil and Environmental Engineering, Georgia Institute of Technology, Atlanta, Georgia, USA.
[4]U.S. Geological Survey, Woods Hole, Massachusetts, USA.

0148-0227/10/2009JB006670

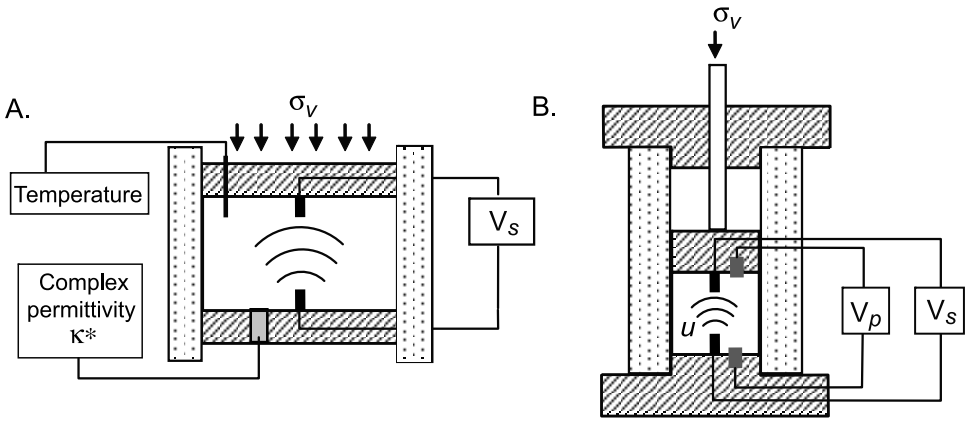

Figure 1. Experimental cells built for the small-strain mechanical measurements. (a) The low fluid pressure odometer cell is described by *Lee et al.* [2010a] and accommodates a specimen 4 to 5 cm high and 10 cm in diameter. (b) The high fluid pressure odometer cell (99.5 mm outer diameter; 60 mm inner diameter; 241.5 mm height) is designed for a specimen 4 to 5 cm high and 6 cm in diameter; *u* denotes pore pressure.

2006] have also been applied to infer gas hydrate distribution and concentration in natural field settings. In many of these studies, the calibration of seismic velocity as a function of gas hydrate concentration is based on an extension of macroscale and microstructural relationships developed empirically for nonhydrate-bearing sediments.

[4] No study has ever attempted to acquire an exhaustive, internally consistent, laboratory data set documenting small-strain mechanical properties over a range of soil types, effective stress conditions, and gas hydrate saturations. Such a data set is a critical first step for proper calibration of field-based seismic data, which are acquired at lower frequency and average over greater length scales than the laboratory data. This paper reports on V_P, V_S, and small-strain Poisson's ratio for such an exhaustive set of experiments, complementing the electromagnetic data reported by *Lee et al.* [2010b] (hereinafter referred to as paper 1), the thermal conductivity results described by *Cortes et al.* [2009], the strength properties given by *Yun et al.* [2007], earlier results on velocities for sands alone detailed by *Yun et al.* [2005], and summary information provided by *Santamarina and Ruppel* [2010].

2. Devices and Methods

[5] Two laboratory cells were designed and built to study hydrate-bearing sediments under zero lateral strain conditions (Figure 1). The low fluid pressure cell operates at atmospheric fluid pressure and was used to gather complex permittivity, compressibility and V_S data. The electromagnetic data acquired on hydrate-bearing sediments with this cell were reported in paper 1. The high-pressure cell can sustain fluid pressure in excess of 20 MPa. The main advantage of this cell is that the high fluid pressure ensures complete liquid saturation, a necessity since P velocity can decrease by an order of magnitude if saturation falls from 100% to 99%. S velocities are less sensitive to small changes in saturation, meaning that they can be properly measured even in the lower pressure cell. Both cells allow a maximum vertical effective stress of $\sigma_v' = 3$ MPa. The specimen height for these cells ranges between 40 mm and 50 mm to obtain adequate compressibility and wave propagation data.

[6] Pinducers (Valpey Fisher, model VP1093) are used to generate and detect P waves. Bender elements, preferred to shear plates for their superior coupling characteristics, are used for S velocity measurements [*Lee and Santamarina*, 2005]. The sensor pairs are installed in the top cap and in the bottom plate of the cells. The source crystals are connected to signal generators, and the signal from the receiver crystals are amplified then digitized and stored using an oscilloscope operating at a sampling rate at least ten times higher than the frequency band of the measurements. The signal generator is also connected to the digital storage oscilloscope so that input and output signals can be compared to determine travel time.

[7] As detailed by *Lee et al.* [2007] and in paper 1, tetrahydrofuran (THF) was selected as the hydrate former for these experiments. This permitted us to form hydrate from dissolved phase and to obtain both well-controlled hydrate saturations and samples that are inferred to be homogeneous.

[8] Soils, specimen preparation, and measurement procedures for the lower pressure cell are described in paper 1. Only a few details differ for the high-pressure cell: (1) The vertical stress σ_v' is applied in four loading steps: 0.04, 0.5, 1, and 2 MPa; (2) the specimen temperature can range between 20°C to −10°C and is controlled by circulating coolant in the chamber that surrounds the cell; and (3) all $S_{hyd} = 0.5$ specimen are prepared with a 60% THF solution to allow for rapid cooling without ice formation (excess THF). Note that for the electromagnetic measurements described in paper 1 it is critical that the $S_{hyd} = 0.5$ specimens have excess water, not excess THF. Thus, the $S_{hyd} = 0.5$ specimens described in paper 1 were formed with a 10%, not 60%, THF solution.

[9] The test sequence for both the low and high fluid pressure cells consists of loading to a predetermined vertical effective stress, cooling to form hydrate, warming to dissociate hydrate, and then loading to next loading stage. Values of V_P and V_S were determined at each stage. A final stage of unloading was imposed on the hydrate-bearing

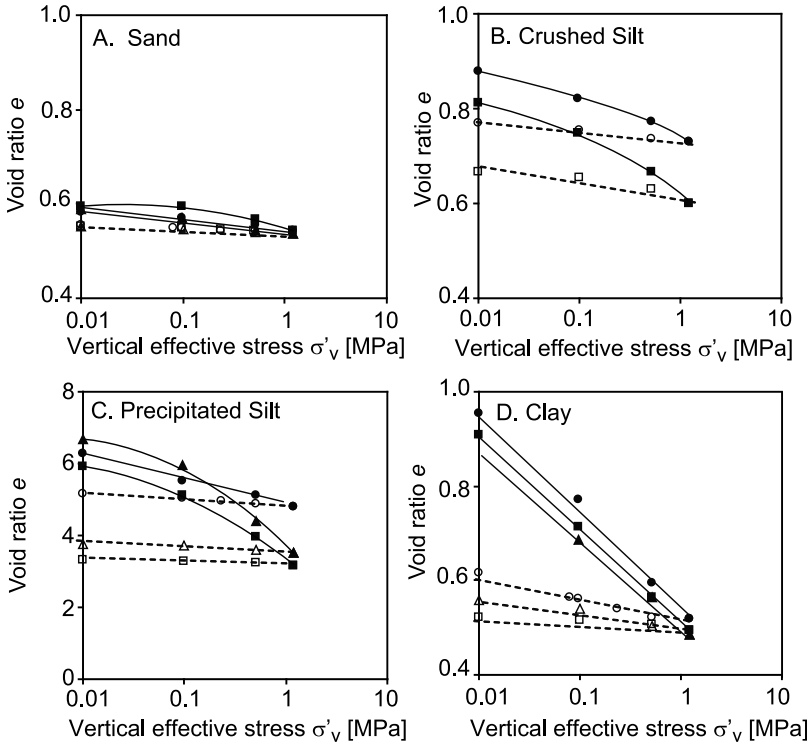

Figure 2. Void ratio versus vertical effective stress for (a) sand, (b) crushed silt, (c) precipitated silt, and (d) clay with pore fluids of deionized water as circles; 10% THF (converts to S_{hyd} = 0.5 after hydrate formation) as triangles; and 21% THF (converts to S_{hyd} = 1.0 after hydrate formation) as squares. The data sets are from low fluid pressure cell. The load is applied at a temperature above the phase transformation to hydrate so that specimens are hydrate-free when loaded (solid line and symbols). Specimens are unloaded (dashed line and open symbols) at a temperature below phase transformation (with hydrates). The loading and unloading "paths" do not truly reflect the experimental sequence, which consisted of loading followed by phase transformation and then unloading within the hydrate stability field at the end of the final loading and hydrate formation cycle. Note that the results for precipitated silt (Figure 2c) are shown on a different scale for void ratio.

specimen within the low-fluid pressure cell following the last loading step in order to study the impact of retrieval of samples from in situ (field) conditions and their analysis at ambient conditions.

3. Results

[10] Test results are summarized next, starting with the evolution of sediment porosity during loading, followed by S and P velocity results. The complete experimental data set is given by *Lee* [2007].

3.1. Compressibility of Sediments Without Hydrates

[11] As shown in paper 1, the sediment porosity n decreases as the vertical effective stress σ'_v increases. Following the standard data reduction approach in geomechanics, Figure 2 shows the porosity cast in terms of void ratio $e = n/(1 - n)$ as a function of applied vertical effective stress σ'_v. The compression index C_c, summarized for these experiments in Table 1, is the slope of the normal consolidation line on a plot of void ratio versus log (σ'_v/1 kPa). The sediment compressibility increases with the specific surface of sedi-

Table 1. Compression Index C_c and Swelling Index C_s for Different Soil Types and for Pore Fluid Mixtures in the Absence of Hydrates

		Compression Index C_c			Swelling Index C_s		
Sediment	Specific Surface	Fluid[a] 0% THF 100% H_2O	Fluid[b] 10% THF 90% H_20	Fluid[c] 21% THF 79% H_2O	Fluid[a] 0% THF 100% H_2O	Fluid[b] 10% THF 90% H_20	Fluid[c] 21% THF 79% H_2O
Sand	0.019	0.02	0.03	0.03	0.01	0.01	0.01
Crushed silt	0.113	0.08	-	0.12	0.03	-	0.03
Clay	36.5	0.21	0.20	0.20	0.05	0.04	0.02
Precipitated silt	120	0.70	1.40	1.40	0.14	0.12	0.05

[a]Corresponds to S_{hyd} = 0 (no hydrate).
[b]Produces S_{hyd} = 0.5 once hydrate forms.
[c]Produces S_{hyd} = 1 once hydrate forms.

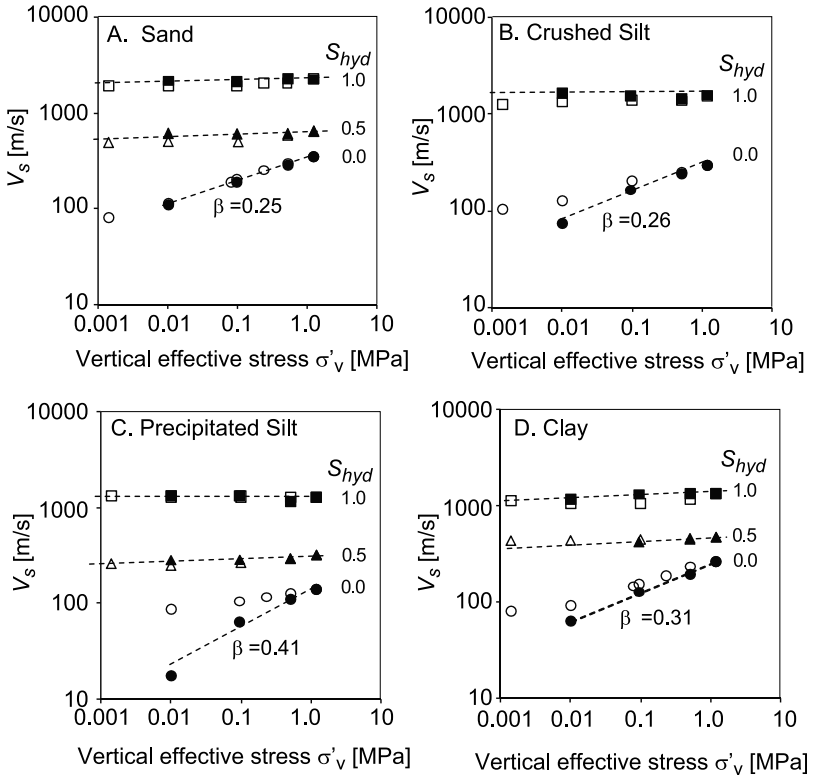

Figure 3. S velocity as a function of vertical effective stress in log-log space for (a) sand, (b) crushed silt, (c) precipitated silt, and (d) clay. The slope β is labeled only for the case of $S_{\mathrm{hyd}} = 0$ (circles). Triangles denote $S_{\mathrm{hyd}} = 0.5$, and squares represent $S_{\mathrm{hyd}} = 1.0$. Solid symbols show the loading path, while open symbols and dashed lines denote the unloading data. The description of loading and unloading "paths" is the same as in Figure 2.

ments (Table 1). Sand and crushed silt specimens have stable fabrics that remain unaltered by applied stress and therefore C_c values are low. Precipitated silt and clay specimens are characterized by high specific surface and exhibit high compressibility. The compressibility is affected by pore fluid permittivity, which decreases with increasing THF concentration (paper 1). While loading is imposed on specimens without hydrates, the hydrate formation-dissociation cycles in the $S_{\mathrm{hyd}} = 0.5$ and 1.0 specimens affect the C_c values for some soils.

[12] We highlight the relevance of specific surface as a single index parameter that captures grain size, the presence of fines in coarse grained sediments, the transition from round coarse particles to platy fine grains, mineralogy (e.g., clay particles have submicron sizes, and each clay mineral has its own range of specific surface), and dual porosity characteristics. Specific surface inherently accounts for fabric development, stiffness-stress relationships [e.g., *Yun et al.*, 2007], and the impact of hydrate formation on sediments.

3.2. Shear Velocity

[13] Contact stiffness between neighboring particles determines the sediment skeletal stiffness, which in turn controls the shear velocity of sediments. The importance of contact stiffness means that we expect a Hertzian-type power relation between velocity and the vertical effective stress to hold in this case: $V_S = \alpha(\sigma'_v/\mathrm{kPa})^{\beta}$ where α and β are fitting parameters and kPa is included as a divisor to render the expression in parentheses unitless. The factor α is the shear wave velocity at $\sigma'_v = 1$ kPa, and the β exponent reflects the nature of contact behavior and the extent of fabric alterations as stress conditions change. This power equation becomes a line when plotted in log-log space, $\log(V_S) = \log\,\alpha + \beta\,\log(\sigma'_v/\mathrm{kPa})$ as in Figure 3. This scale also allows us to compare V_S values that range over nearly 2 orders of magnitude. Because the V_S data acquired with the high fluid pressure cell superimpose on those from the low-pressure cell, we show only the low-pressure V_S data. The shear stiffness of soils without hydrates ($S_{\mathrm{hyd}} = 0.0$) increases with the vertical effective stress, and the slope β is greater in high specific surface sediments than in low specific surface sediments.

[14] Figure 3 shows that the S velocities are much higher for hydrate-bearing specimens than for the same specimens having only water as the pore filling material. V_S is less than 650 m s^{-1} in all sediments and at all stress levels when $S_{\mathrm{hyd}} \leq 0.5$; however V_S reaches 1200 to 2300 m s^{-1} in sediments with $S_{\mathrm{hyd}} = 1.0$. The S velocity increases with hydrate saturation owing to an increase in skeletal shear stiffness. For experiments in sands with fine increments in S_{hyd}, the transition in shear stiffness occurs at $S_{\mathrm{hyd}} \approx 0.4$ [*Berge et al.*, 1999; *Yun et al.*, 2005], a transition also inferred by *Guerin and Goldberg* [2002] based on analysis

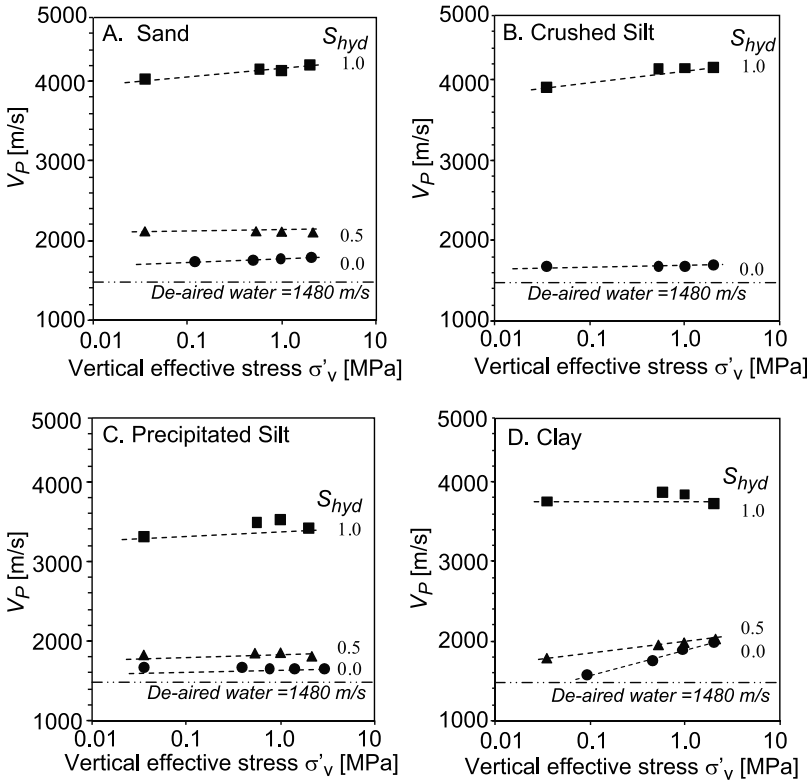

Figure 4. P velocity as a function of vertical effective stress in log linear space for (a) sand, (b) crushed silt, (c) precipitated silt, and (d) clay. Hydrate saturation S_{hyd} is indicated by circles for 0, triangles for 0.5, and squares for 1.0. Data are shown only for the loading step. V_p for de-aired water is provided for reference. Dashed lines show data trends, not best fits. Note that these data were collected only in the high-pressure cell.

of borehole sonic logs. At higher S_{hyd}, which includes data presented here for S_{hyd} = 0.5 and 1, the presence of hydrates has a significant impact on shear stiffness and becomes more important than the stiffening effect associated with the vertical effective stress. At high hydrate saturations, the small strain shear stiffness becomes insensitive to changes in the vertical effective stress. In fact, β is approximately zero for S_{hyd} = 1.0. Implications of these results are explored further in section 4.3.

3.3. Compressional Velocity

[15] The compressional velocity for water saturated sediments is controlled by the bulk modulus of the water phase. Thus, the V_P results for the specimens with S_{hyd} = 0, shown in Figure 4, start near the velocity for de-aired water (V = 1480 m s^{-1}), and exhibit a minor increase with increasing vertical effective stress due to decreased porosity and increased sediment skeletal stiffness during consolidation. There is some increase in V_P when the hydrate concentration increases from 0 to 0.5 and a pronounced increase when the hydrate concentration changes from 0.5 to 1. The results for sand, precipitated silt and clay shown in Figure 4 are in agreement with earlier data reported by *Yun et al.* [2005], which also demonstrated no major change in V_s of sands until hydrate saturation exceeded ~0.4.

3.4. Unloading Data

[16] Unloading of the specimens, which was conducted at low temperatures to preserve the hydrates for the S_{hyd} = 0.5 and 1.0 samples, results in volume expansion, as shown in Figure 2. The swelling index C_s is the slope of the decompression line on the plot of void ratio e versus the logarithm of the effective stress σ'_v plot. Calculated C_s values are summarized in Table 1. C_s varies little across the range of S_{hyd} values for low specific surface soils (sand). C_s is larger for higher specific surface sediments and increases with decreasing S_{hyd}. This means that volume expansion during unloading is restricted at high hydrate saturation [e.g., *Lee et al.*, 2010a].

[17] Figure 3 shows V_S values for samples in their loaded and unloaded states. The values of V_S are higher during unloading than during loading in sediments without hydrates due to the higher interparticle coordination and locked-in strain when sediments have been preloaded. With a few exceptions, V_S remains almost constant during the unloading of hydrate-bearing specimens with S_{hyd} = 0.5 and 1.0.

4. Discussion

[18] The propagation velocity of small-strain elastic waves is determined by the medium's stiffness and mass den-

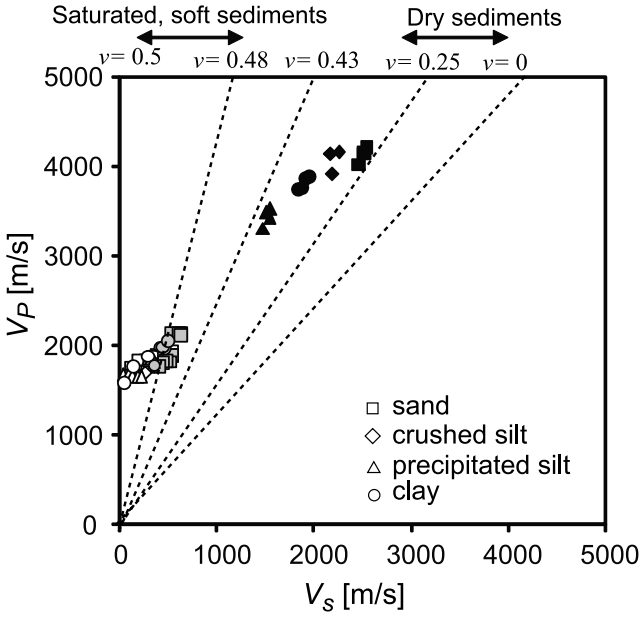

Figure 5. Small-strain Poisson's ratio inferred from V_P and V_S for S_{hyd} = 0 (open symbols), S_{hyd} = 0.5 (gray symbols), and S_{hyd} = 1.0 (solid symbols), with the soil type as given by the legend. Data obtained at all effective stress levels are plotted here.

sity ρ [kg m^{-3}]. The small-strain wave propagation velocities can be expressed in terms of the bulk modulus B [Pa], the constraint modulus M [Pa], and the shear modulus G [Pa] using standard expressions from elasticity:

$$V_P = \sqrt{\frac{M}{\rho}} = \sqrt{\frac{B + \frac{4}{3}G}{\rho}}, \tag{1}$$

$$V_S = \sqrt{\frac{G}{\rho}}, \tag{2}$$

$$\frac{V_P}{V_S} = \sqrt{\frac{M}{G}} = \sqrt{\frac{2(1-\nu)}{1-2\nu}}, \tag{3}$$

where ν is the small-strain Poisson's ratio of the medium. These expressions allow us to study the effect of hydrates on the small strain Poisson's ratio and the bulk modulus.

4.1. Small-Strain Poisson's Ratio

[19] The small-strain Poisson's ratio ν of dry sediments is very small (e.g., 0.05 to 0.15) because deformations localize at interparticle contacts and the fabric remains constant [*Santamarina et al.*, 2001]. At the other extreme are liquid-saturated soft sediments where $B \gg G$ and ν approaches 0.5. Figure 5 shows our V_P and V_S data, with superposed curves corresponding to different values of small-strain Poisson's ratio according to (3). Results show the evolution from a fluid-controlled bulk modulus where ν approaches 0.5 for specimens subject to low vertical effective stress and lacking hydrate, to high skeletal stiffness where ν approaches 0.25 at increasing vertical stress and particularly when S_{hyd} = 1.0. We underscore that these results give small-strain values of Poisson's ratio for the water-saturated sediment, rather than for the granular skeleton, and should not be used for the analysis of large-strain drained processes in hydrate-bearing sediments. For other reasons, we have advised caution in extrapolating large-strain experimental results on hydrate-bearing sediments to Poisson's ratio in natural settings [*Yun et al.*, 2007].

4.2. Bulk Modulus

[20] Using (1) and (2), the bulk modulus of the hydrate-bearing sediment B_{hbs} can be calculated using the measured V_P and V_S values, as shown in Figure 6. We can also estimate bounds for the bulk modulus of hydrate-bearing sediments knowing the volume fraction and bulk moduli of components and assuming their spatial arrangement. Extreme bounds for B_{hbs} can be computed as the arithmetic mean and the harmonic mean. The Hashin-Shtrikman (hereafter HS) bounds [*Hashin and Shtrikman*, 1963] shown in Figure 6 assume either that the stiffest (upper bound) or the softest (lower bound) components form shells around the other components. The bulk moduli of the individual components for our specimens (e.g., water, hydrate, and soil grains) are superimposed on Figure 6 as reference values. The results demonstrate that the bulk modulus of hydrate-bearing sediments is limited by the soft components and remains near the lower HS bound for $S_{hyd} \leq 0.5$. The presence of hydrates filling the pore space when $S_{hyd} \approx 1.0$ causes a pronounced change in the interaction among components, and the bulk modulus B_{hbs} moves toward the upper HS bound.

4.3. Material Models

[21] Velocity-stress trends for sediments without hydrates allow us to extract the α and β parameters in the power expression $V_S = \alpha(\sigma'_v/\text{kPa})^\beta$ from section 3.2. Experimentally determined β values show that $\beta = 0$ in solids, β approaches 0 for cemented soils, the Hertzian β = 1/6 is obtained with densely packed round sands, $\beta \approx 0.25$ for rough or angular sand and silt particles (specific surface range < 0.1 m^2 g^{-1}), $\beta \approx 0.30$ for low-plasticity clays (specific surface range ~ 10 m^2 g^{-1}), and $\beta \geq 0.40$ in high-plasticity clays (specific surface range > 100 m^2 g^{-1}) [*Santamarina et al.*, 2001]. For sediments lacking hydrates, the β values we obtain from analysis of our data are in agreement with these reference values (Figure 3). In particular, the high β value for precipitated silt is consistent with the high initial porosity and pronounced compressibility during loading, as observed in Figure 2c.

[22] For hydrate-bearing sediments, we chose a general model that resembles the mathematical form of theoretical expressions for cemented soils [*Fernandez and Santamarina*, 2001] and that combines the stress-dependent sediment response with the stiffness of the hydrate mass [*Santamarina and Ruppel*, 2010]:

$$V_S = \sqrt{\left(\frac{V_{hyd} S_{hyd}^2}{n}\right)^2 \theta + \left[\alpha\left(\frac{\sigma'_v + \sigma'_h}{2\ \text{kPa}}\right)^\beta\right]^2}, \tag{4}$$

where the factor θ reflects the microstructural relationship between hydrate and the grains and the α and β values are

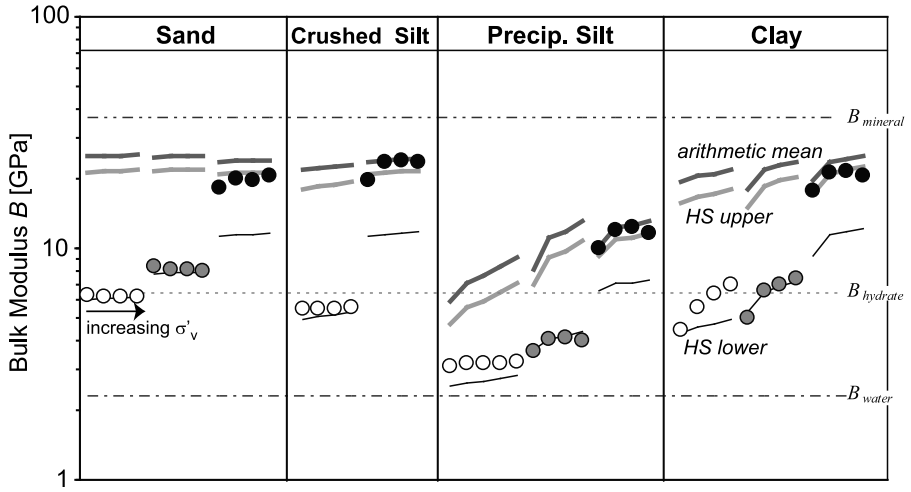

Figure 6. Bulk moduli of hydrate-bearing sediments B_{hbs} computed using the measured V_P and V_S values for (from left to right) sand, crushed silt, precipitated silt, and clay. Open circles denote S_{hyd} = 0.0, gray circles correspond to S_{hyd} = 0.5, and solid circles represent S_{hyd} = 1.0. Each set of 4 or 5 measurements within a single S_{hyd} value for each soil correspond to vertical effective stress from 0.04 to 2.12 MPa, ordered in terms of increasing vertical stress to the right. Thin black curves show lower HS bounds, which are the same as the harmonic mean. Light gray and dark gray curves correspond to upper HS bounds and the arithmetic mean, respectively. These bounds were computed using volume fractions and the properties of components (hydrate, water, and mineral) as denoted by the dashed lines. The bulk modulus of the sediment skeleton B_{sk} is computed from $G_{sk} = V_S^2\rho$ assuming ν_{sk} = 0.15.

extracted from tests conducted on sediments lacking hydrates. Measured and predicted V_S for all specimens we tested are plotted in Figure 7a. In all cases, we find $\theta \leq 0.15$ for our experiments forming hydrate from dissolved phase THF. *Santamarina and Ruppel* [2010] note that θ should be substantially larger for hydrate formed in the presence of a gas phase in unsaturated media.

[23] As discussed by *Yun et al.* [2005], the measured V_P should not be used to determine V_S for water-saturated hydrate-bearing sediments. Measurement errors in V_P near low values of S_{hyd} are magnified in the estimation of V_S [*Yun et al.*, 2005]. Conversely the measured V_S can be combined with the bulk modulus for each component to calculate V_P based on a Biot-Gassmann type formulation. For low stiffness B_{sk} of the skeleton relative to mineral grain bulk modulus B_m, V_P can be written as

$$V_P^2 = V_S^2\left[\frac{4}{3}+\frac{2(1+\nu_{sk})}{3(1-2\nu_{sk})}\right]+\frac{1}{\rho}\left[\frac{n(1-S_{\mathrm{hyd}})}{B_w}+\frac{nS_{\mathrm{hyd}}}{B_{\mathrm{hyd}}}+\frac{1-n}{B_{\mathrm{min}}}\right]^{-1}, \tag{5}$$

where subscripts hbs, w, min, and hyd denote the hydrate-bearing sediment, water, mineral grains, and hydrate, respectively, and ν_{sk} is the small strain Poisson's ratio for the skeleton, which is typically 0.1 ± 0.05. Equation (5) is modified from *Santamarina et al.* [2001] to include hydrate. Measured V_P and V_P predicted from (5) are plotted in Figure 7b.

4.4. Hydrate Formation Technique and Seismic Velocities

[24] Many researchers have used effective media models to predict the small-scale mechanical properties of saturated sediments with and without gas hydrates [e.g., *Chand et al.*, 2006; *Digby*, 1981; *Dvorkin et al.*, 1994; *Helgerud et al.*, 1999; *Jakobsen et al.*, 2000; *Walton*, 1987]. For the analysis of field-scale seismic data, studies typically adopt Wyllie's macroscale time-averaged empirical equation [*Wyllie et al.*, 1958] and infer hydrate saturation, thereby inherently assuming a particular microstructural relationship among sediment grains, pore fluid, and gas hydrate [*Bangs et al.*, 1993; *Korenaga et al.*, 1997; *Lee and Collett*, 2001; *Lee et al.*, 1996; *Wood et al.*, 1994].

[25] In practical terms, the cementation model, in which gas hydrate grows at grain contacts, leads to rapid increases in both V_P and V_S with increasing S_{hyd}, even for small values of S_{hyd}. A model in which gas hydrate grows within the pores (pore filling model) produces no appreciable increase in V_S with increasing S_{hyd} until S_{hyd} is large enough that gas hydrate begins to affect both the skeletal stiffness (important for V_S) and the bulk modulus (important, along with skeletal stiffness, for V_P). An intermediate model in which gas hydrate nucleates on grains and grows into pore space was proposed by *Yun et al.* [2005, 2007] to explain small-strain data from sands and large-strain data from a range of sediment types, respectively. This model produces minor cementation and increases in V_S for $S_{\mathrm{hyd}} \leq 0.4$ since hydrate rarely forms at the contacts between grains in the absence of a free gas phase [*Yun et al.*, 2005].

[26] The pattern of V_P and V_S changes as a function of S_{hyd} can be used to compare various laboratory studies and demonstrate the differences in velocities related to hydrate formation method. Figure 8 shows the measured velocity data for sands at all values of vertical effective stress for this study, along with data from other hydrate-bearing sand studies and theoretical curves for various models of hydrate

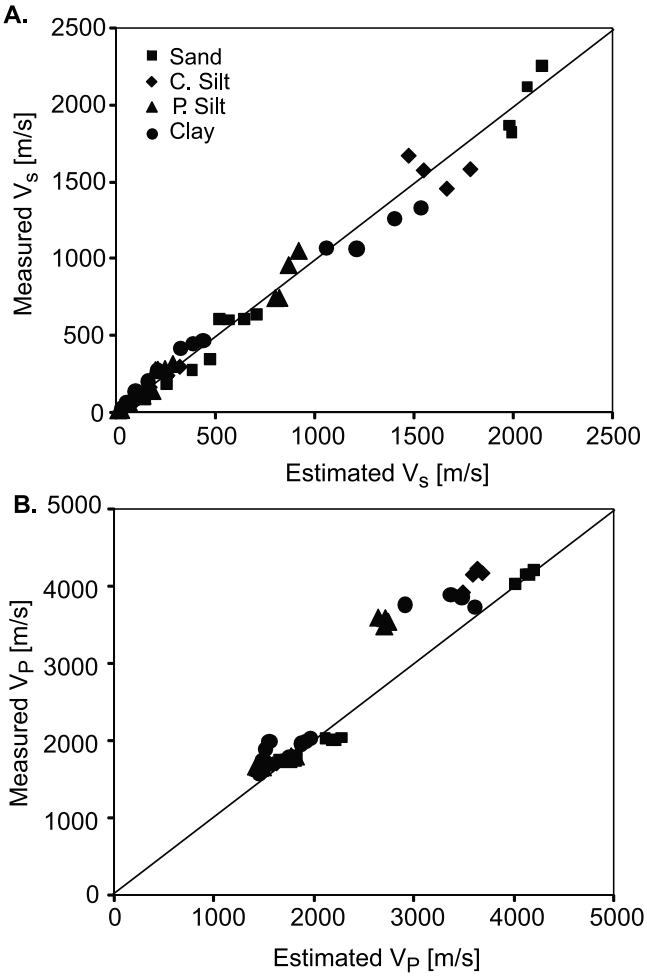

Figure 7. Validation of predictive models given by equations (4) and (5) for (a) V_S and (b) V_P. Measured versus estimated velocities are shown for all soils (symbols as given in the legend), hydrate saturations, and vertical effective stress levels. Parameters are α = 80 m s^{-1}, β = 0.25, and θ = 0.15 for sand; α = 50 m s^{-1}, β = 0.26, and θ = 0.12 for crushed silt; α = 10 m s^{-1}, β = 0.41, and θ = 0.13 for precipitated silt; and α = 23 m s^{-1}, β = 0.31, and θ = 0.07 for clay.

distribution with respect to grains within sediments [*Lee*, 2007].

[27] The velocity data for hydrate synthesized in soils by percolating gas through unsaturated sediments [*Winters et al.*, 2005] agrees well with the cementation model that predicts a significant increase in small-strain skeletal stiffness with relatively small amounts of hydrate. Gas hydrate formed in this way tends to develop at the menisci between grains, thereby cementing the grains. Likewise, the formation of hydrate by the ice seed method of *Stern et al.* [1996] and *Priest et al.* [2005] preferentially forms hydrate at grain contacts. As the ice melts, water clings to mineral surfaces and contacts, which become the nucleation sites for methane hydrate growth. This leads to an early increase in skeletal stiffness.

[28] Small-strain stiffness does not increase significantly until $S_{hyd} > 0.4$ [*Yun et al.*, 2005] in specimens synthesized by flushing saturated soils with water containing a dissolved phase hydrate former. In this case, hydrates tend to nucleate on grain surfaces and grow into the pore space. The P wave velocity results of *Spangenberg and Kulenkampff* [2005], obtained with dissolved methane as the hydrate former, are also shown in Figure 8 for comparison with the THF results. When the hydrate volume fraction exceeds $S_{hyd} > 0.4$, the hydrate mass touches more than one particle and can contribute to interparticle coordination, skeletal stability and

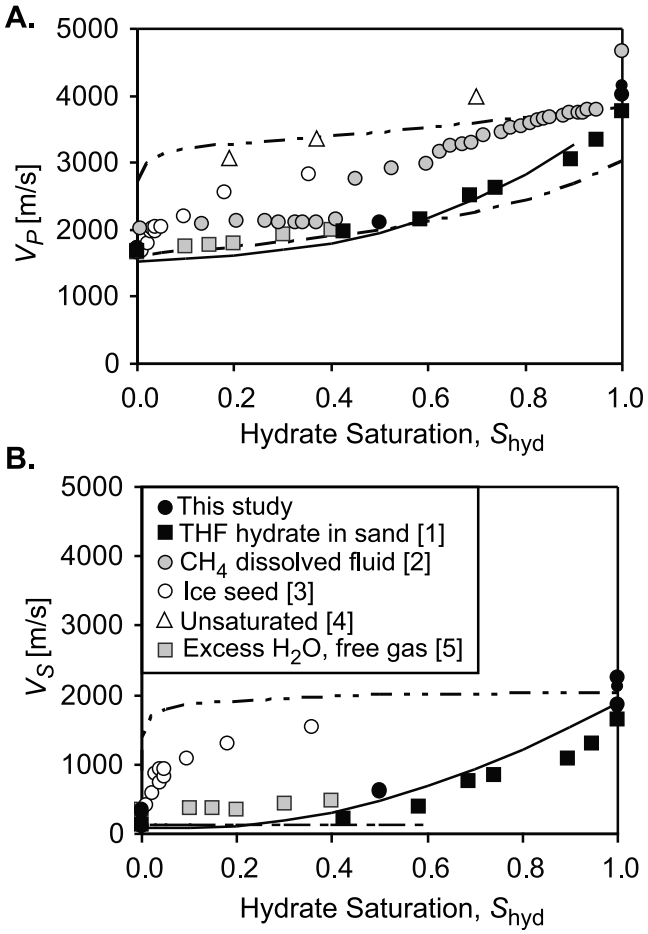

Figure 8. The impact of hydrate formation method on measured P and S velocities in hydrate-bearing sediments. References are (1) *Yun et al.* [2005] for THF hydrate with no effective vertical stress; (2) *Spangenberg and Kulenkampff* [2005] for CH_4 hydrate formed from dissolved phase, with the vertical effective stress unspecified; (3) *Priest et al.* [2005] for CH_4 hydrate formed from ice seed with σ'_v = 590 kPa; (4) *Winters et al.* [2005] for CH_4 hydrate formed in unsaturated condition with σ'_v = 230~270 kPa; (5) *Priest et al.* [2009] for CH_4 hydrate formed with excess water method with σ'_v = 500 kPa. The solid theoretical curve was computed using (4) for V_S and (5) for V_P assuming α = 80 m/s, β = 0.25, θ = 0.15, B_{hyd} = 5.6 GPa, B_{min} = 36 GPa, B_w = 2.0 GPa, G_{hyd} = 2.4 GPa, and G_{min} = 45 GPa. The pore-filling model (dash-dotted curve) was computed at σ'_v = 0.01 MPa. The cementation model (dash-double dotted curve) was computed at σ'_v = 2.1 MPa. The pore-filling model and the cementation model suggested by *Dvorkin and Nur* [1996] are used to calculate theoretical curves.

stiffness [*Yun et al.*, 2005]. Specimens with hydrate formed in excess water and free gas by *Priest et al.* [2009] behave similar to those with hydrate formed with dissolved methane, since hydrate starts to form around gas bubbles, which reside in the pore space.

[29] Based on the comparison of trends obtained with THF [*Yun et al.*, 2005; this study] and those obtained with dissolved methane by *Spangenberg and Kulenkampff* [2005], we conclude that the nucleation and growth of THF hydrate are similar to those of methane hydrate formed from dissolved phase, particularly at low S_{hyd}.

4.5. Unloading Data: Simulating Pressure Coring

[30] When vertical effective stress on a specimen is reduced, the specimen expands, causing tension on cementing agents at grain contacts. This often produces an irrecoverable reduction in stiffness, a phenomenon commonly observed in cemented soils subjected to decreased vertical effective stress [*Baig et al.*, 1997; *Fernandez and Santamarina*, 2001].

[31] The unloading data presented in section 3.4 and Figure 2 can be used to explore the impact of decreased vertical effective stress on hydrate-bearing sediments. The experimental conditions that produce a drastic reduction in vertical effective stress without dissociation of the hydrate represent a good analogy for coring hydrate-bearing sediments using pressure coring methods. During modern pressure coring as carried out within the Integrated Ocean Drilling Program and other deepwater drilling expeditions [e.g., *Schultheiss et al.*, 2008], cores ~1 m long are retrieved from hydrate-bearing sediments with the complete release of vertical effective stress ($\sigma'_v \approx 0$) but maintenance of the pore fluid (hydrostatic) pressure. In field applications, pressure core temperatures are often not maintained within the hydrate stability field during core recovery (except in the corer described by *Takahashi and Tsuji* [2005]), but cores are quickly chilled upon reaching the ship. In our laboratory experiments, temperatures are maintained within the hydrate stability field during the entire unloading history.

[32] The volume expansion and S velocity data shown in Figures 2 and 3 for the unloading cycle indicate that, for $S_{hyd} \geq 0.5$, the presence of hydrate in the specimens hinders swelling and locks in stiffness, at least during the 2 h (sand and crushed silt) to 4 day (clay and precipitated silt) duration of these unloading tests. In field settings, retrieval of a pressure core would take a maximum of a few hours, meaning that sediments with intermediate saturations of hydrate could largely retain their structure as long as the core remains within the hydrate stability field. Note that our data set includes specimens with only three values of S_{hyd} (0, 0.5, and 1), so we cannot determine the hydrate saturation that marks the transition between sediments that will be strongly affected by the release of vertical effective stress and those that may maintain their structural integrity during retrieval. We suspect that the transition likely coincides with $S_{hyd} \approx 0.4$, which our previous work has shown to be a saturation level that is associated with a marked increase in skeletal stiffness, at least in sands [*Yun et al.*, 2005].

[33] These unloading results suggest that the probability of sampling hydrate-bearing sediments without disturbing the original sediment fabric increases when the in situ vertical effective stress is low, sediments have low specific surface, and the hydrate saturation is high. A similar conclusion was reached by *Lee et al.* [2008], who studied synthetic hydrates formed in natural sediments from the deepwater Gulf of Mexico. In all cases, the specimen should be restored to the in situ fluid pressure, vertical effective stress, and temperatures within the hydrate stability field as soon as possible to minimize hydrate dissociation, fluid migration, and later hydrate reformation in new locations within the core.

5. Conclusions

[34] Systematic experiments conducted on sand, silts, and clay specimens containing synthetic (THF) hydrate formed from dissolved phase to obtain pore-space hydrate saturations of 0, 0.5, and 1 and subject to vertical effective stress ranging from 0.04 to 2 MPa reveal the following:

[35] 1. The small-strain properties of hydrate-bearing sediments are governed by the state of effective stress, hydrate saturation, and the soil's specific surface. In this context, specific surface is a single soil index that captures grain size, mineralogy and related particle level interactions.

[36] 2. The S velocity increases with hydrate saturation owing to an increase in skeletal shear stiffness. For experiments in sands subjected to minimal vertical effective stress and with fine increments in S_{hyd}, the transition in shear stiffness occurs at $S_{hyd} \approx 0.4$. At higher S_{hyd}, which includes data presented here for $S_{hyd} = 0.5$ and 1, the presence of hydrates has a significant impact on shear stiffness and becomes more important than the stiffening effect associated with the vertical effective stress. At these elevated hydrate saturations, the small strain shear stiffness also becomes insensitive to changes in the vertical effective stress.

[37] 3. The P velocity increases with hydrate saturation due to the increase in both the bulk modulus of pore-filling phases due to fluid-to-hydrate conversion and the shear modulus of the skeleton.

[38] 4. The small-strain Poisson's ratio approaches $\nu \approx 0.5$ in water-saturated sediments with neither gas nor hydrates and subjected to a low vertical effective stress. When the vertical effective stress is high and in particular when the hydrate saturation is high, the sediment exhibits high skeletal stiffness and Poisson's ratio may decrease to $\nu = 0.25$. These values of Poisson's ratio are applicable only to small-strain conditions and cannot be used to analyze the large-strain drained response of hydrate-bearing sediments.

[39] 5. The bulk modulus of hydrate-bearing sediments is limited by soft components and remains near the Hashin-Shtrikman (HS) mixture lower bound for $S_{hyd} \leq 0.5$. However, the presence of hydrates filling the pore space at $S_{hyd} \approx 1.0$ causes a pronounced change in the interaction among components, and the bulk modulus B_{hbs} moves toward the HS mixture upper bound.

[40] 6. The laboratory technique used to form hydrate has a significant impact on the rate that V_P and V_S increases with increasing S_{hyd}. Based on this paper and our previous work, we infer that formation of hydrate by bubbling gas through unsaturated sediment will lead to rapid increase in V_S at low S_{hyd}. Hydrate formation using ice seeds also leads to rapid rates of V_P and V_S changes with increasing S_{hyd}. Hydrate formation from dissolved phase leads to slower V_P and V_S increases with increasing S_{hyd} Hydrate nucleates on grain

surfaces and initially grows into pores before grains become interconnected for $S_{hyd} \geq 0.4$ [e.g., *Yun et al.*, 2005].

[41] 7. Mathematical relationships based on mechanistic concepts, not mere fitting, are proposed to estimate S and P velocity as a function of the hydrate saturation, vertical effective stress, and sediment-dependent parameters (e.g., specific surface).

[42] 8. At $S_{hyd} \geq 0.5$, the presence of hydrate in sediments hinders expansion and stiffness degradation during the reduction of vertical effective stress, as long as the temperature and fluid pressure are maintained within the hydrate stability field. This finding implies that in situ fabric and sediment characteristics may be preserved when recovering pressure cores from sediments with high hydrate saturation.

[43] **Acknowledgments.** Initial support for this research to J.C.S. and C.R. at Georgia Tech was provided by the Chevron Joint Industry Project on Methane Hydrates under contract DE-FC26-01NT41330 from the U.S. Department of Energy. Additional support to J.C.S. was provided by the Goizueta Foundation at Georgia Tech and to J.Y.L. by KIGAM, GHDO, and MKE. We thank W. Waite and B. Dugan for comments that improved the manuscript. Any use of a trade, product, or firm name is for descriptive purposes only and does not imply endorsement by the U.S. Government. Any opinions, findings, conclusions, or recommendations expressed herein are those of the authors and do not necessarily reflect the view of the DOE or the USGS.

References

Baig, S., M. Picornell, and S. Nazarian (1997), Low strain shear moduli of cemented sands, *J. Geotech. Eng.*, *123*, 540–545.

Bangs, N. L. B., D. S. Sawyer, and X. Golovchenko (1993), Free gas at the base of the gas hydrate zone in the vicinity of the Chile Triple Junction, *Geology*, *21*, 905–908, doi:10.1130/0091-7613(1993)021<0905:FGATBO>2.3.CO;2.

Bathe, M., S. Vagle, G. A. Saunders, and E. F. Lambson (1984), Ultrasonic wave velocities in the Structure-II clathrate hydrate $THF{\cdot}17H_2O$, *J. Mater. Sci. Lett.*, *3*, 904–906, doi:10.1007/BF00719584.

Bauer, K., R. G. Pratt, C. Haberland, and M. Weber (2008), Neural network analysis of crosshole tomographic images: The seismic signature of gas hydrate bearing sediments in the Mackenzie Delta (NW Canada), *Geophys. Res. Lett.*, *35*, L19306, doi:10.1029/2008GL035263.

Berge, L. I., K. A. Jacobsen, and A. Solstad (1999), Measured acoustic wave velocities of R11($CC_{l3}F$) hydrate samples with and without sand as a function of hydrate concentration, *J. Geophys. Res.*, *104*, 15,415–15,424, doi:10.1029/1999JB900098.

Chand, S., T. A. Minshull, J. A. Priest, A. I. Best, C. R. I. Clayton, and W. F. Waite (2006), An effective medium inversion algorithm for gas hydrate quantification and its application to laboratory and borehole measurements of gas hydrate-bearing sediments, *Geophys. J. Int.*, *166*, 543–552, doi:10.1111/j.1365-246X.2006.03038.x.

Cortes, D. D., A. I. Martin, T. S. Yun, F. M. Francisca, J. C. Santamarina, and C. Ruppel (2009), Thermal conductivity of hydrate-bearing sediments, *J. Geophys. Res.*, *114*, B11103, doi:10.1029/2008JB006235.

Dai, J., F. Snyder, D. Gillespie, A. Koesoemadinata, and N. Dutta (2008), Exploration for gas hydrate in the deepwater, northern Gulf of Mexico: Part 1. A seismic approach based on geologic model, inversion, and rock physics principles, *Mar. Pet. Geol.*, *25*, 830–844, doi:10.1016/j.marpetgeo.2008.02.006.

Digby, P. J. (1981), The effective elastic-moduli of porous granular rocks, *J. Appl. Mech.*, *48*, 803–808, doi:10.1115/1.3157738.

Dvorkin, J., and A. Nur (1996), Elasticity of high-porosity sandstones: Theory for two North Sea datasets, *Geophysics*, *61*, 1363–1378, doi:10.1190/1.1444059.

Dvorkin, J., A. Nur, and H. Z. Yin (1994), Effective properties of cemented granular-materials, *Mech. Mater.*, *18*, 351–366, doi:10.1016/0167-6636(94)90044-2.

Fernandez, A., and J. C. Santamarina (2001), The effect of cementations on the small strain parameters of sands, *Can. Geotech. J.*, *38*, 191–199, doi:10.1139/cgj-38-1-191.

Guerin, G., and D. Goldberg (2002), Sonic waveform attenuation in gas hydrate-bearing sediments from the Mallik 2L-38 research well, Mackenzie Delta, Canada, *J. Geophys. Res.*, *107*(B5), 2088, doi:10.1029/2001JB000556.

Hardage, B. A., D. Sava, M. M. Backus, R. Remington, R. Graves, R. Graebner, and H. H. Roberts (2006), Evaluation of deep-water gas hydrate systems, *Leading Edge*, *25*, 572–576, doi:10.1190/1.2202661.

Hashin, Z., and S. Shtrikman (1963), A variational approach to the elastic behavior of multiphase materials, *J. Mech. Phys. Solids*, *11*, 127–140, doi:10.1016/0022-5096(63)90060-7.

Helgerud, M. B., J. Dvorkin, A. Nur, A. Sakai, and T. Collett (1999), Elastic-wave velocity in marine sediments with gas hydrates: Effective medium modeling, *Geophys. Res. Lett.*, *26*, 2021–2024, doi:10.1029/1999GL900421.

Holbrook, W. S., H. Hoskins, W. T. Wood, R. A. Stephen, and D. Lizarralde, and the Leg 164 Science Party (1996), Methane hydrate and free gas on the Blake Ridge from vertical seismic profiling, *Science*, *273*, 1840–1843, doi:10.1126/science.273.5283.1840.

Jakobsen, M., J. A. Hudson, T. A. Minshull, and S. C. Singh (2000), Elastic properties of hydrate-bearing sediments using effective medium theory, *J. Geophys. Res.*, *105*, 561–577, doi:10.1029/1999JB900190.

Kiefte, H., M. J. Clouter, and R. E. Gagnon (1985), Determination of acoustic velocities of clathrate hydrates by Brillouin spectroscopy, *J. Phys. Chem.*, *89*, 3103–3108, doi:10.1021/j100260a031.

Korenaga, J., W. S. Holbrook, S. C. Singh, and T. A. Minshull (1997), Natural gas hydrates on the southeast U.S. margin: Constraints from full waveform and travel time inversions of wide-angle seismic data, *J. Geophys. Res.*, *102*, 15,345–15,365, doi:10.1029/97JB00725.

Kumar, D., M. K. Sen, and N. L. Bangs (2007), Gas hydrate concentration and characteristics within Hydrate Ridge inferred from multicomponent seismic reflection data, *J. Geophys. Res.*, *112*, B12306, doi:10.1029/2007JB004993.

Lee, J.-S., and J. C. Santamarina (2005), Bender elements: Performance and signal interpretation, *J. Geotech. Geoenviron. Eng.*, *131*, 1063–1070, doi:10.1061/(ASCE)1090-0241(2005)131:9(1063).

Lee, J. Y. (2007), Hydrate-bearing sediments: Formation and geophysical properties, Ph.D. thesis, 226 pp., Ga. Inst. of Technol., Atlanta.

Lee, J. Y., T. S. Yun, J. C. Santamarina, and C. Ruppel (2007), Observations related to tetrahydrofuran and methane hydrates for laboratory studies of hydrate-bearing sediments, *Geochem. Geophys. Geosyst.*, *8*, Q06003, doi:10.1029/2006GC001531.

Lee, J. Y., J. C. Santamarina, and C. Ruppel (2008), Mechanical and electromagnetic properties of northern Gulf of Mexico sediments with and without THF hydrates, *Mar. Pet. Geol.*, *25*, 884–895.

Lee, J. Y., J. C. Santamarina, and C. Ruppel (2010a), Volume change associated with formation and dissociation of hydrate in sediment, *Geochem. Geophys. Geosyst.*, *11*, Q03007, doi:10.1029/2009GC002667.

Lee, J. Y., J. C. Santamarina, and C. Ruppel (2010b), Parametric study of the physical properties of hydrate-bearing sand, silt, and clay sediments: 1. Electromagnetic properties, *J. Geophys. Res.*, *115*, B11104, doi:10.1029/2009JB006669.

Lee, M. W. (2002), Biot-Gassmann theory for velocities of gas hydrates-bearing sediments, *Geophysics*, *67*, 1711–1719, doi:10.1190/1.1527072.

Lee, M. W., and T. S. Collett (2001), Elastic properties of gas hydrate-bearing sediments, *Geophysics*, *66*, 763–771, doi:10.1190/1.1444966.

Lee, M. W., D. R. Hutchinson, T. S. Collett, and W. P. Dillon (1996), Seismic velocities for hydrate-bearing sediments using weighted equation, *J. Geophys. Res.*, *101*, 20,347–20,358, doi:10.1029/96JB01886.

Pandit, B. I., and M. S. King (1982), Elastic wave velocities of propane gas hydrates, paper presented at Canadian Permafrost Conference.

Pearson, C., J. Murphy, and R. Hermes (1986), Acoustic and resistivity measurements on rock samples containing tetrahydrofuran hydrates: Laboratory analogs to natural-gas hydrate deposits, *J. Geophys. Res.*, *91*, 14,132–14,138, doi:10.1029/JB091iB14p14132.

Priest, J. A., A. I. Best, and C. R. I. Clayton (2005), A laboratory investigation into the seismic velocities of methane gas hydrate-bearing sand, *J. Geophys. Res.*, *110*, B04102, doi:10.1029/2004JB003259.

Priest, J. A., E. V. L. Rees, and C. R. I. Clayton (2009), Influence of gas hydrate morphology on the seismic velocities of sands, *J. Geophys. Res.*, *114*, B11205, doi:10.1029/2009JB006284.

Santamarina, J. C., and C. Ruppel (2010), The impact of hydrate saturation on the mechanical, electrical, and thermal properties of hydrate-bearing sand, silts, and clay, in *Geophysical Characterization of Gas Hydrates*, *Geophys. Dev. Ser.*, vol. 14, edited by M. Riedel, E. C. Willoughby, and S. Chopra, pp. 373–384, Soc. Exploration Geophysics, Tulsa, Okla.

Santamarina, J. C., K. A. Klein, and M. A. Fam (2001), *Soils and Waves*, 488 pp., John Wiley, New York.

Schultheiss, P., M. Holland, and G. Humphreys (2008), Borehole pressure coring and laboratory pressure core analysis for gas hydrate investigations, paper 19601 presented at Offshore Technology Conference, Houston, Tex.

Spangenberg, E., and J. Kulenkampff (2005), Physical properties of gas hydrate-bearing sediments, paper presented at 5th International Conference on Gas Hydrates, Trondheim, Norway, 12–16 June.

Stern, L. A., S. H. Kirby, and W. B. Durham (1996), Peculiarities of methane clathrate hydrate formation and solid-state deformation, including possible superheating of water ice, *Science*, *273*, 1843–1848, doi:10.1126/science.273.5283.1843.

Stoll, R. D. (1974), Effects of gas hydrates in sediments, in *Natural Gases in Marine Sediments*, edited by I. R. Kaplan, pp. 235–248, Plenum, New York.

Stoll, R. D., and G. M. Bryan (1979), Physical-properties of sediments containing gas hydrates, *J. Geophys. Res.*, *84*, 1629–1634, doi:10.1029/JB084iB04p01629.

Stoll, R. D., J. Ewing, and G. M. Bryan (1971), Anomalous wave velocities in sediments containing gas hydrates, *J. Geophys. Res.*, *76*, 2090–2094, doi:10.1029/JB076i008p02090.

Takahashi, H., and Y. Tsuji (2005) Multi-well exploration program in 2004 for natural hydrate in the Nankai-trough offshore Japan, paper 17162 presented at Offshore Technology Conference, Houston, Tex.

Tinivella, U., and J. M. Carcione (2001), Estimation of gas-hydrate concentration and free-gas saturation from log and seismic data, *Leading Edge*, *20*, 200–203, doi:10.1190/1.1438914.

Walton, K. (1987), The effective elastic-moduli of a random packing of spheres, *J. Mech. Phys. Solids*, *35*, 213–226, doi:10.1016/0022-5096(87)90036-6.

Westbrook, G. K., et al. (2008), Estimation of gas hydrate concentration from multi-component seismic data at sites on the continental margins of NW Svalbard and the Storegga region of Norway, *Mar. Pet. Geol.*, *25*, 744–758, doi:10.1016/j.marpetgeo.2008.02.003.

Winters, W. J., L. Y. Gilbert, D. H. Mason, I. A. Pecher, and W. F. Waite (2005), Effect of grain size and pore pressure on acoustic and strength behavior of sediments containing methane gas hydrate, paper presented at Fifth International Conference on Gas Hydrates, Trondheim, Norway, 12–16 June.

Wittebolle, R. J., and D. C. Sego (1985), A laboratory facility for testing sediments containing gas hydrates, paper presented at Fourth International Offshore Mechanics and Arctic Engineering Symposium, Am. Soc. of Chem. Eng., New York.

Wood, W. T., P. L. Stoffa, and T. H. Shipley (1994), Quantitative detection of methane hydrate through high-resolution seismic velocity analysis, *J. Geophys. Res.*, *99*, 9681–9695, doi:10.1029/94JB00238.

Wyllie, M. R. J., A. R. Gregory, and G. H. F. Gardner (1958), An experimental investigation of factors affecting elastic wave velocities in porous media, *Geophysics*, *23*, 459–493, doi:10.1190/1.1438493.

Yun, T. S., F. M. Francisca, J. C. Santamarina, and C. Ruppel (2005), Compressional and shear wave velocities in uncemented sediment containing gas hydrate, *Geophys. Res. Lett.*, *32*, L10609, doi:10.1029/2005GL022607.

Yun, T. S., J. C. Santamarina, and C. Ruppel (2007), Mechanical properties of sand, silt, and clay containing tetrahydrofuran hydrate, *J. Geophys. Res.*, *112*, B04106, doi:10.1029/2006JB004484.

Zillmer, M. (2006), A method for determining gas-hydrate and free-gas saturation of porous media from seismic measurements, *Geophysics*, *71*, N21–N32, doi:10.1190/1.2192910.

F. M. Francisca, Ingenieria Civil, Universidad Nacional de Cordoba, Cordoba 5000, Argentina. (ffrancis@com.uncor.edu)

J. Y. Lee, Petroleum and Marine Resources Division, Korea Institute of Geoscience and Mineral Resources, 92 Gwahang-no, Yuseong-gu, Deajeon 305-350, South Korea. (jyl@kigam.re.kr)

C. Ruppel, U.S. Geological Survey, 384 Woods Hole Rd., Woods Hole, MA 02543, USA. (cruppel@usgs.gov)

J. C. Santamarina, School of Civil and Environmental Engineering, Georgia Institute of Technology, 790 Atlantic Dr., Atlanta, GA 30332-0355, USA. (jcs@ce.gatech.edu)